



1 **Surface area and Ω -aragonite oversaturation as controls of the**
2 **runaway precipitation process in ocean alkalinity enhancement**

3
4 **Niels Suitner¹, Jens Hartmann¹, Selene Varliero², Giulia Faucher³, Philipp Suessle³, and Charly A. Moras¹**

5
6 ¹Institute for Geology, University of Hamburg, Bundesstrasse 55, 20146 Hamburg, Germany

7 ²Department of Chemistry, Materials and Chemical Engineering “Giulio Natta”, Politecnico di Milano,
8 Milan; Italy

9 ³GEOMAR Helmholtz Centre for Ocean Research Kiel, Wischhofstrasse 1-3, 24148 Kiel, Germany

10

11 Correspondence: Niels Suitner (niels.suitner@uni-hamburg.de),

12 Jens Hartmann (geo@hates.de)

13

14 **Orcid:**

15 Niels Suitner: <https://orcid.org/0000-0003-3413-857X>

16 Jens Hartmann: <https://orcid.org/0000-0003-1878-9321>

17 Selene Varliero: <https://orcid.org/0000-0001-9532-2202>

18 Giulia Faucher: <https://orcid.org/0000-0001-8930-477X>

19 Philipp Suessle: <https://orcid.org/0000-0001-7224-2330>

20 Charly A. Moras: <https://orcid.org/0000-0001-6819-6167>



21 **Abstract**

22 Ocean alkalinity enhancement (OAE) is a strategy for marine carbon dioxide removal that aims to increase the
23 total alkalinity (TA) of seawater to sequester atmospheric CO₂ in the form of dissolved inorganic carbon (DIC).
24 An intense alkalization of seawater resulting from OAE treatment could trigger a significant runaway carbonate
25 precipitation process, which may lead to a loss of initially added alkalinity, thereby limiting its efficiency. Even
26 under natural background aragonite saturation states, a continuous yet barely detectable loss of alkalinity is
27 theoretically expected to occur in seawater. With the additional increase through OAE, time ranges to initiate an
28 appreciable TA loss process could be reduced significantly. Therefore, predicting the alkalinity stability ranges
29 might be a necessity for application scenarios. The main drivers of the precipitation process are i) the aragonite
30 saturation state of seawater and ii) the available surface area for heterogeneous precipitation.

31 In this study, we refined the use of logistic functions to describe the temporal evolution of both drivers, with
32 experimental datasets using natural seawater from the Raunefjorden (Bergen, Norway; Temp.: ~11°C, Sal.: ~32.6).
33 The observed patterns were then used to derive a process-based model for calculating TA-loss rates, focusing on
34 the accelerated precipitation phase of the runaway process while considering saturation levels and available
35 particle surface area. The formation of carbonate phases reduces seawater TA concentrations, inducing a delay or
36 stopping the TA-loss process. In addition, the sinking of precipitated particles decreases the potential for further
37 precipitation by reducing the available surface area in the system. To assess the impact of particle sinking on TA-
38 loss, their shape and size distribution were determined. Under the environmental conditions presented here, TA-
39 loss rates could be reduced by up to 30-40% due to the sinking of particles, after just one day.

40 Integrating the proposed concepts into ocean models could enhance the accuracy of predictions regarding the fate
41 of added alkalinity. Gaining insights into the evolution of the identified, seemingly stable TA levels can help
42 prevent accelerated precipitation phases. Additionally, an understanding of particle sinking or dilution processes
43 reducing the available reactive particle surface area is relevant to assess the efficacy and durability of OAE.

44



45 1 Introduction

46 To mitigate climate change and reach net-zero greenhouse gas emissions by the end of the century, negative
 47 emission technologies (NETs) are necessary (UNFCCC, 2015) considering the slow change in the development
 48 of the energy infrastructure, lifestyle of humanity, and national goals for economic growth (Fuss et al., 2018; Iyer
 49 et al., 2015; Sers & Victor, 2018). Various carbon dioxide removal (CDR) technologies have been proposed to
 50 help achieve the necessary negative emission trajectories (Hartmann et al., 2013; IPCC, 2023; Minx et al., 2018;
 51 Rogelj et al., 2018). Among these, ocean alkalinity enhancement (OAE) is a promising CDR method (Harvey,
 52 2008; Ilyina et al., 2013; Kheshgi, 1995; Rau & Caldeira, 1999), with the potential to geochemically sequester 3-
 53 30 Gt CO₂ yr⁻¹ (Oschlies et al., 2023; Renforth & Henderson, 2017).

54 Alkalinity enhancement could be achieved by two addition approaches: **1.** a non-CO₂-equilibrated (neq) or **2.** a
 55 CO₂-equilibrated (eq) (Schulz et al., 2023). Through the neq approach, alkaline materials, such as silicate or
 56 hydroxide-based mineral phases could be introduced to seawater in the form of solids or solutions, allowing longer-
 57 term CO₂ equilibration with the atmosphere through ingassing of atmospheric CO₂. In the eq approach, already
 58 partially pre-CO₂-equilibrated solutions or carbonate-based substances could be released into seawater. Neq
 59 alkalinity addition strategies induce greater variations in the affected carbonate system, resulting in drastically
 60 reduced *p*CO₂ and a rapid increase in pH values. While an eq alkalinity addition results in less severe changes in
 61 ocean chemistry, it is less efficient in generating carbon sequestration potential (Schulz et al., 2023; Suitner et al.,
 62 2024).

63 Depending on the introduced alkalization method (see Eisaman et al., 2023) and the magnitude of treatment,
 64 induced changes in the carbonate system could lead to adverse effects on biota (Faucher et al., 2024; Ferderer et
 65 al., 2022; Gately et al., 2023; Goldenberg et al., 2024; Marín-Samper et al., 2024; Sánchez et al., 2024; Xin et al.,
 66 2024) or in case of persistent oversaturation, result in the precipitation of secondary mineral phases and therefore
 67 a loss of the introduced total alkalinity (TA) (Ilyina et al., 2013; Schulz et al., 2023). The process of TA leakage as
 68 a consequence of OAE was recently described by several studies (see Fuhr et al., 2022; Hartmann et al., 2023;
 69 Moras et al., 2022; Pan et al., 2021; Ringham et al., 2024; Suitner et al., 2024; Varliero et al., 2024). Within these
 70 laboratory-based studies, self-sustaining runaway carbonate precipitation processes led to a significant decrease in
 71 the added alkalinity, which could even result in a net-loss of TA. TA stability ranges, and the evolution of the
 72 precipitation process depend on the specific local environmental conditions such as temperature, salinity, aragonite
 73 saturation state (Ω_{ar}), or suspended particle load of the treated water mass (Moras et al., 2024).

74 The objective of this study is to demonstrate the general capability to predict and parametrize the temporal
 75 evolution of a triggered runaway carbonate precipitation process during OAE approaches, based on quantifiable
 76 and measurable parameters. Estimations of stability ranges for the permanence of introduced alkalinity additions
 77 were derived from these parametrizations. The ability to predict TA stability ranges can help prevent secondary
 78 mineral formation and optimize assessments for future OAE application scenarios.

79 Suitner et al. (2024) demonstrated the potential of utilizing inverse logistic functions to depict the temporal
 80 evolution of the TA-loss process during the runaway carbonate formation phase (see Fig. 1). In this study, principal
 81 descriptive parameters such as TA addition and stability ranges to trigger the runaway process or the timespan of
 82 the precipitation phase could be formalized based on their experimental dataset. This approach also offers the
 83 possibility of a straightforward integration of time-dependent loss terms into predictive computational models



84 simulating OAE addition scenarios, as presented by He & Tyka (2023), Ou et al. (2025), Schwinger et al. (2024)
85 or Zhou et al. (2024).
86 The application of OAE may exceed critical levels for carbonate precipitation. For open ocean scenarios the rapid
87 initiation of mixing processes would efficiently reduce the potential for secondary carbonate formation.
88 Nevertheless, runaway carbonate formation may occur within enclosed geographic locations with physical features
89 such as bays, estuaries, or lagoons. In addition, thermohaline layering (Bialik et al., 2022) or high sediment load
90 (Wurgaft et al., 2016, 2021) might create conditions that lead to alkalinity loss processes.
91 To sustain the observed runaway carbonate formation (Fig. 1), it is essential to retain the precipitates in the system.
92 Removal of these particles reduces the potential for continuous heterogeneous precipitation, thereby slowing down
93 or halting the process. In this study, the empirically determined alkalinity loss rates were used to derive the quantity
94 of precipitated particles. By identifying the particle sizes, shapes, densities, and sinking velocities, their potential
95 residence times in the water column were estimated. Furthermore, we evaluated whether the formation of
96 secondary minerals can supply sufficient surface area for a continuous detectable heterogeneous runaway process
97 in an open-water body and whether the process would be interrupted or attenuated by removing particles due to
98 their descent into deeper layers.

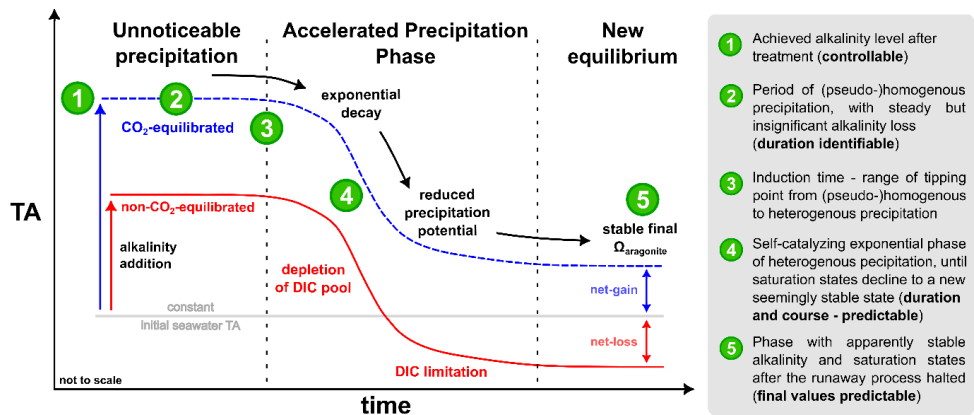


Figure 1: Modified conceptual scheme of a runaway carbonate precipitation process following liquid alkalinity addition after Fig. 9 in Suimer et al., 2024 (not to scale)



2 Material and methods

2.1 Overview of experimental setups

Three incubation experiments were conducted to examine the stability of alkalinity of the local “filtered” (mesh size 0.2 μm) and “unfiltered” (mesh size 50 μm) seawater of the Raunefjorden, Norway (60.27° N, 5.20° E). Within TA-gradient approaches, runaway precipitation was observed in eq and neq treatments, after surpassing specific time and alkalinity addition ranges, allowing the description of patterns during the precipitation process. A detailed description of the experimental results, design and methods is already given in Suitner et al. (2024), a brief overview is also provided in Tab. 1.

Table 1: Overview of the experimental design of precipitation experiments in Suitner et al. (2024)

#	filter mesh size	CO ₂ state to atmosphere	Alkaline material	Runtime [days]	Range TA _{added} [$\mu\text{mol kg}^{-1}$]	TA _{added} gradient steps [$\mu\text{mol kg}^{-1}$]	Temperature [°C]
I	50 μm	non-equilibrated (neq)	NaOH	25	0-2800	200	10-11
II	0.2 μm				0-3400		11-13
III	0.2 μm	air-equilibrated (eq)	Na ₂ CO ₃ /NaHCO ₃	20	0-9200	800	12-16

2.2 Curve fitting of the TA and Ω_{ar} evolution

The numerical curve fit model to describe the temporal development of TA and Ω_{ar} , as presented in Suitner et al. (2024), was refined by additionally including the observed TA-loss rates as a second input factor, to provide continuous functions as a basis for further model calculations. The curve fit model utilized the consistent tendency of all observed runaway precipitation processes to follow inverse logistic trends in form of:

$$f(t) = a e^{-b e^{-c t}} + d \quad (1)$$

for the temporal evolution of TA and Ω_{ar} . The coefficients (**d**) and (**a**) are defined by the achieved level of TA/ Ω_{ar} after the addition (**d**) and the final reached value after the runaway process halted (**a**). Since these factors are predefined by the experimental setup, the curve fit model only numerically parameterizes the two coefficients (**b**) and (**c**). Coefficient (**b**) represents the “induction time”, or the time required for CaCO₃ precipitation to become detectable in the TA measurements, depicted by the horizontal translation along the x-axis, while (**c**) denotes the timespan between start and end of an accelerated precipitation phase (APP). See Fig. 2 for a visual impression of the influence of iterations of each coefficient.

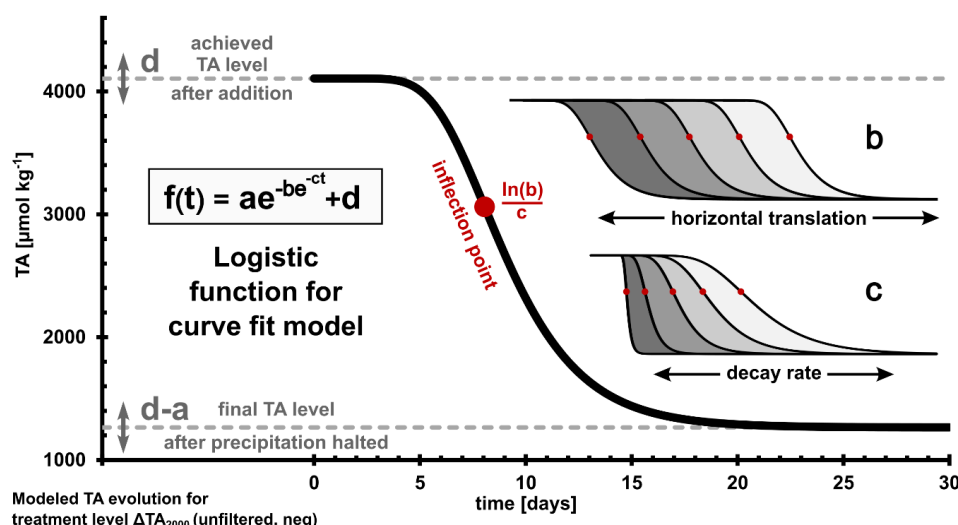


Figure 2: Overview and iterations of each coefficient (a)-(d) of the applied inverse logistic function for the numerical curve fitting; the inflection point is defined by $\ln(b)/c$; for further characteristics see Tjørve & Tjørve (2017)

123

124 2.3 Empirical rate law and determination of loss rates

125 A simple empirical rate law was used to evaluate the precipitation rates R [$\mu\text{mol m}^{-2} \text{h}^{-1}$] (see e.g. Inskeep &
 126 Bloom, 1985; Morse et al., 2007; Zhong & Mucci, 1989):

$$127 \quad R = k(\Omega_{ar} - 1)^n \quad (2)$$

128 The experimental TA-loss rates were then fitted to the logarithmic form of Eq. (2) to determine the coefficients k
 129 (rate constant) and n (empirical reaction order):

$$130 \quad \log(R) = n(\Omega_{ar} - 1) + \log(k) \quad (3)$$

131 To correct for the variable surface area, r [$\mu\text{mol h}^{-1}$] was normalized for the assumed available active mineral
 132 surface area (A in [m^2]) (adapted from Sjöberg, 1976).

$$133 \quad r = k A (\Omega_{ar} - 1)^n \quad (4)$$

134 As the gradient approaches could not provide a sufficient amount of precipitates to determine their surface area, a
 135 one-week side experiment was conducted to estimate the mineral surface area generated during the runaway
 136 precipitation process. By adding 3.8 mmol NaOH and 7.0 mmol NaHCO_3 to 40 L of natural seawater (salinity 33)
 137 at 23°C, around 5 g of aragonite precipitates were generated to provide material for a BET surface area
 138 measurement. Using N_2 adsorption (Brunauer et al., 1938), with a Quantachrome autosorb iQ at the University of
 139 Hamburg, a surface area of $2.283 \text{ m}^2 \text{g}^{-1}$ was determined. By the assumption that the surface area is constant for
 140 all precipitates and that the entire lost TA is transformed into aragonite particles, the experimentally determined
 141 TA-loss was used to calculate the surface area after each timestep, therefore allowing to correct the precipitation
 142 rates.

143



144 **2.4 Particle analysis**

145 The precipitated particles of three filters, collected during incubation experiments within previous campaigns
146 published in Hartmann et al. (2023) (neq ΔTA_{2400} , Gran Canaria) and Suitner et al. (2024) (neq ΔTA_{2600} and
147 ΔTA_{2800} , Raunefjorden), were analyzed by scanning electron microscopy (SEM; Tabletop Microscope Hitachi
148 TM4000plus - University of Hamburg) to determine shape, size and quantity of the precipitated material. Length,
149 width and shape of each particle were specified by manual examination.
150 If sufficient precipitated materials could be provided, the remaining SEM filter material was used to determine
151 their sinking velocities, utilizing a FlowCam (Fluid Imaging Technologies Inc., Scarborough, United States). A
152 detailed description of the setup is provided in Suessle et al. (2023) and references therein.



153 3 Results

154 3.1 Numerical logistic curve-fittings

155 Three OAE gradient approaches by Suitner et al. (2024) were examined to test the stability of alkalinity and to
 156 generate refined numerical logistic curve fittings of the temporal development of TA and Ω_{ar} (Figs. 3, S2 and S3).
 157 The coefficients (b) and (c) (see Fig. 2) were determined by numerical interpolation to optimize the fit to Eq. (1)
 158 and its derivative in equal proportions. Therefore, the shown functions were optimized to describe the temporal
 159 evolution, while also including the rate loss changes, which allowed an improved description of the runaway
 160 process in comparison to the approaches in Suitner et al. (2024). Outlying data points displaying an anomalous
 161 increase or stagnation in values were removed from curve-fitting calculations (see SI in Suitner et al., 2024). For
 162 each treatment, continuous differentiable functions to describe and analyze the runaway carbonate precipitation
 163 process during OAE approaches were generated. To illustrate the described processes and trends, the unfiltered
 164 neq approach was selected as an example (Fig. 3). The plots for the filtered approaches are provided in the SI
 165 (Figs. S2 and S3).

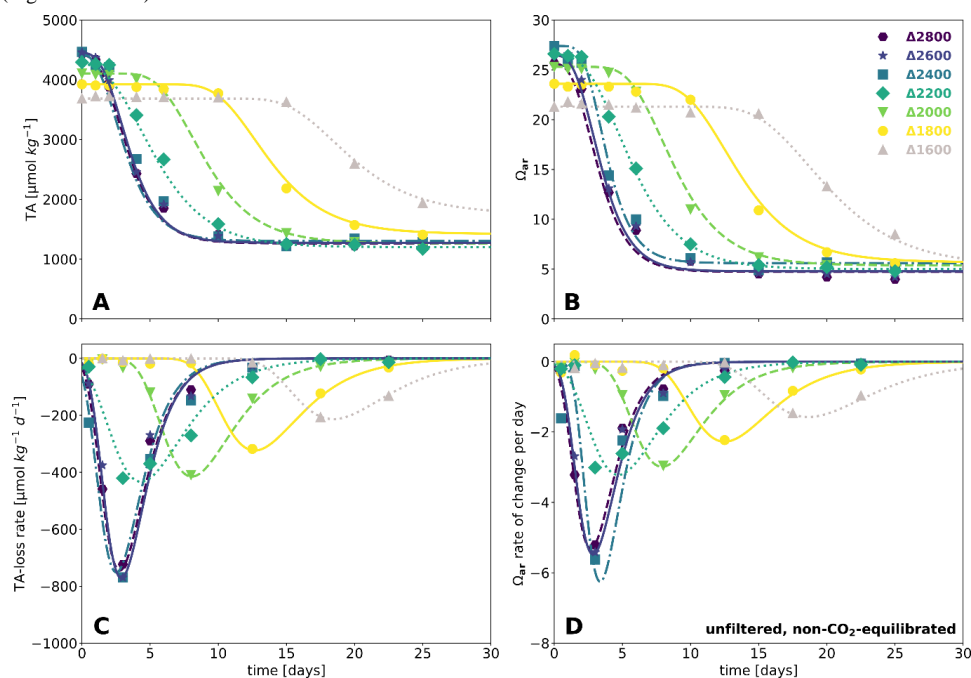


Figure 3: Results of the numerical curve fits – for the unfiltered neq approach, TA evolution over time (A), Ω_{ar} evolution over time (B), TA-loss rate over time (C), Ω_{ar} rate of change over time (D). line plots: curve-fitted continuous functions, markers: measured data points, for related diagrams for filtered approaches see Figs. S2 and S3

166

167 For the unfiltered neq experiment (Fig. 3), treatment levels ΔTA_{1600} and higher entered into an APP after exceeding
 168 critical TA levels to initiate the runaway carbonate precipitation process. Treatments levels $\Delta TA_{2400-2600}$ exhibited
 169 a buffering as a consequence of magnesium hydroxide precipitation (see Badjatya et al., 2022; Ringham et al.,
 170 2024; Suitner et al., 2024; Varliero et al., 2024), which prevented an increase above $\sim 4470 \mu\text{mol kg}^{-1}$ in TA and



~27.4 in Ω_{ar} . The buffering effects were not recognized within the fitting procedure and the first data point (after ~3 min runtime) of each treatment level was set as the baseline.

173

174 **3.2 Induction time and timespan of the APP**

By employing the logistic curve fits, the temporal evolution of each approach could be parameterized. To identify the temporal stability ranges and reflect the transition from stable to precipitation-dominated system modes, a criterion of $40 \mu\text{mol kg}^{-1} \text{d}^{-1}$ rate of change in TA was set. This rate provides a sufficiently high threshold to exclude a false detection due to natural variability or measurement errors, while still being low enough not to overlook a significant fraction of alkalinity loss (see Fig. S9 for varying criteria).

Based on this criterion, Fig. 4 illustrates the induction times for the APPs. The shaded ranges indicate extrapolated timeframes between subsequent measurements during which the initiation of the APP for each treatment was detected. The displayed regressions were calculated using the averaged times from two consecutive measurement days. For comparison, hollow markers represent predictions from the presented curve-fitted functions. The regressions of the induction times uniformly follow an inverse exponential trend of the type:

$$t(TA) = f e^{-g TA} - h \quad (5)$$

The employed data series covered a range of 25 days with progressively increasing induction times from 0 to 20 days for treatments reaching ~4470 (ΔTA_{2400}) to ~3380 $\mu\text{mol kg}^{-1}$ (ΔTA_{1200}) in the filtered neq experiment and ~11200 (ΔTA_{9200}) to ~6500 $\mu\text{mol kg}^{-1}$ (ΔTA_{4400}) in the filtered eq experiment. Treatment levels above ΔTA_{2400} in the neq approaches exhibited an immediate onset of TA-loss due to the precipitation of secondary hydroxides and/or carbonate minerals, therefore, following the presented criterion, practically leading to their immediate entry into the APP process.

The same relationships and trends can also be applied using Ω_{ar} as a variable. While the neq approaches exhibited lower Ω_{ar} values (17.8-27.4) compared to the eq treatments (19.5-43.6), the onset of the APP in the neq experiments occurred significantly earlier. This indicates that Ω_{ar} is not the only decisive factor guiding the (pseudo-) homogeneous nucleation process, determining the induction time.

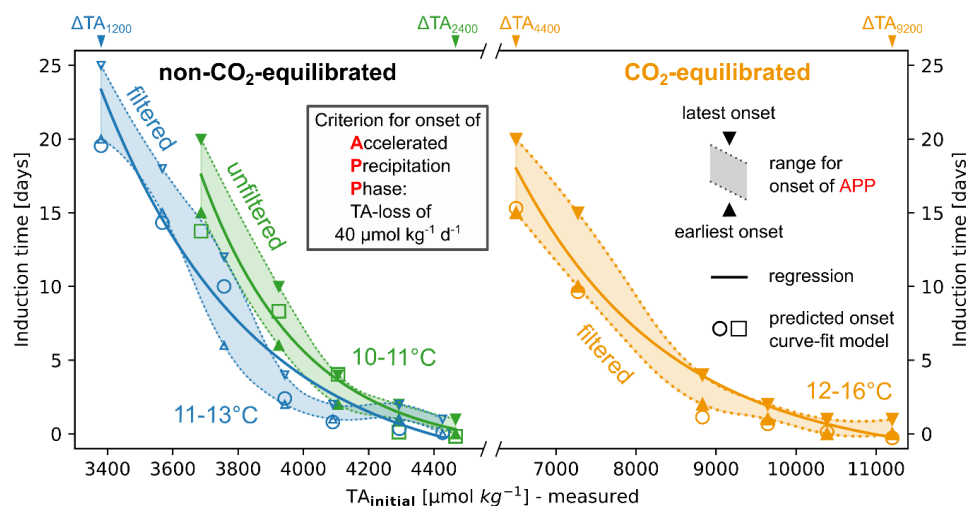


Figure 4: Induction time for the onset of APP in relation to the initial TA addition level, based on the first detection of a TA-loss rate of $40 \mu\text{mol kg}^{-1} \text{d}^{-1}$. Each pair of triangle markers represents two consecutive measurement days during which the set loss rate criterion was met; hollow markers: predicted induction times for each treatment level, based on the introduced curve-fit model. Exponential regression of average experimentally detected induction time, see Eq. (5) in Tab. 2 for related functions

Table 2: Regressions of induction times, see Fig. 4. Note that the use of the given equation should not be generalized, as it is only valid under the presented environmental conditions. Also be aware that the resulting predictions of induction times far out of the specified TA addition ranges might not be accurate.

$t(TA_{\text{initial}}) = f e^{-g TA_{\text{initial}}} - h$ (5)			Regression			
Treatment		Temp. [°C]	$f * 10^3$	$g * 10^{-4}$	h	R^2
non-equilibrated	unfiltered	10-11	2721.769	32.233	1.215	0.996
	filtered	11-13	39.633	21.646	2.972	0.977
equilibrated	filtered	12-16	0.603	5.243	1.934	0.988

3.3 Timespan of APP

To describe the temporal evolution of TA and Ω_{ar} during the observed runaway processes for the present setups, coefficients (a) and (d) in Eq. (1) can be set, while (b) could be evaluated by empirical or modeled data. Consequently, only the duration of the APP represented by (c) needs to be estimated to enable the entire model description of the precipitation procedure. The discrete nature of sampling days with decreasing frequency of samplings towards the end of an experiment (up to 5 days) did not allow reliable empirical determinations of (c). The displayed APP timespans in Fig. 5 were therefore determined by the predictions of the presented curve-fits (Fig. 3), based on the $40 \mu\text{mol kg}^{-1} \text{d}^{-1}$ TA-loss criterion to define the start and endpoint of the APPs. Fig. 5 illustrates the related predicted timespans against the initially reached TA levels, categorized by the individual experimental setups. The neq APPs form distinct clusters for each approach, which again can be subdivided into treatments with and without the occurrence of immediate precipitation. Regardless of the initial TA enhancement level, treatments that exhibited an immediate decline due to $\text{Mg}(\text{OH})_2$ formation showcased almost identical APP



spans (unfiltered ~8.8 and filtered ~5.9-7.4 days) within each approach. Although the neq treatments without $\text{Mg}(\text{OH})_2$ had the same starting conditions, the unfiltered experiments exhibited approximately 4 days longer APPs. APPs in the eq approach showed a continuous increase ranging from 5 to 11 days.

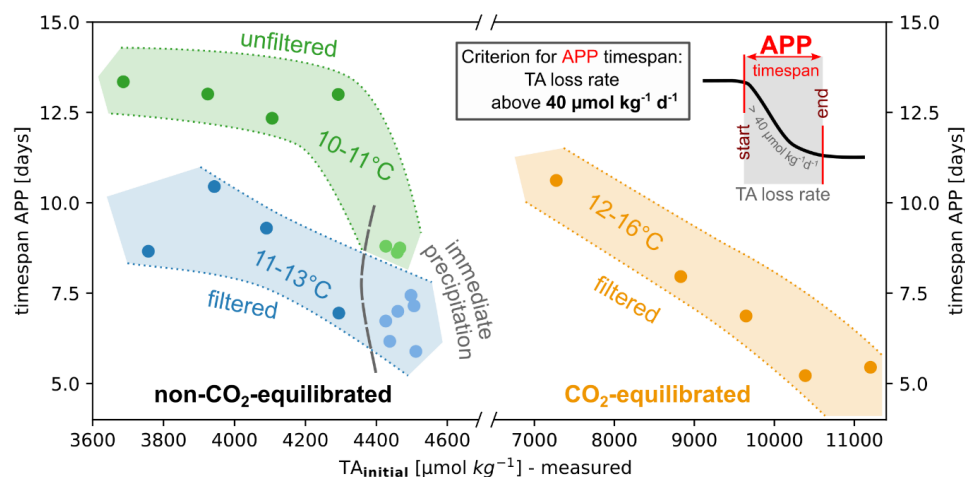


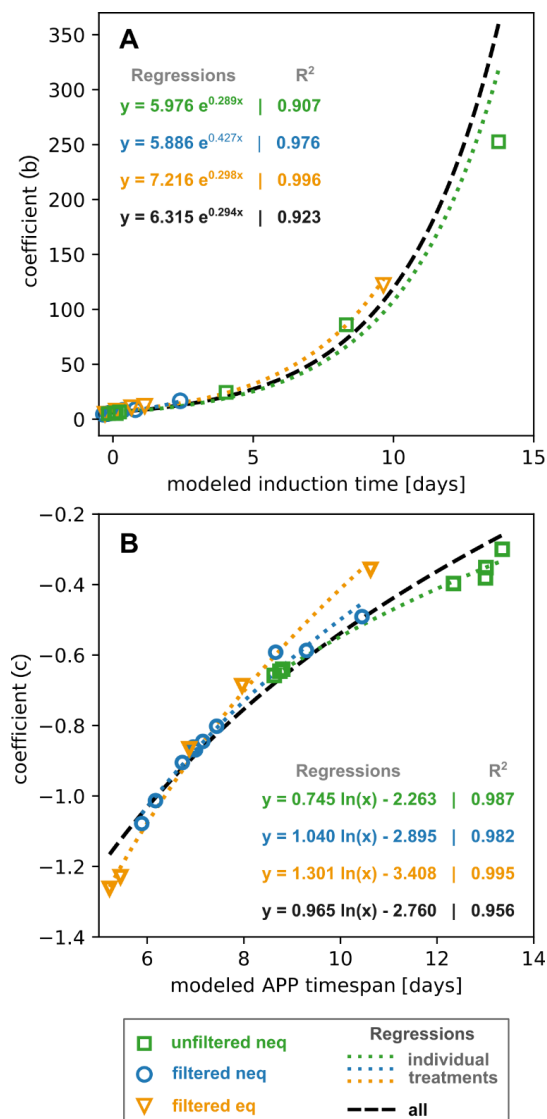
Figure 5: Overview timespans of APP in relation to the initial TA addition level; determined by the outcomes of the presented numerical logistic curve-fitting. Presented timespans are based on the introduced alkalinity loss criterion (see section 3.2), which was defined as period with rates above $40 \mu\text{mol kg}^{-1} \text{d}^{-1}$; only treatments which reached the final stable stage were considered, neq treatments labeled with immediate precipitation showcased a loss of TA within the first 3 min of the experiment – most likely as a consequence of $\text{Mg}(\text{OH})_2$ formation (see Suiter et al., 2024)

3.4 Prediction of onset and timespan of APP

The established continuous logistic functions allow estimations of effects occurring between measurement points, thereby improving the overall accuracy beyond what discrete experimental datasets could provide. Based on the $40 \mu\text{mol kg}^{-1} \text{d}^{-1}$ TA-loss criterion (see section 3.2 and sketch Fig. 5), these functions could therefore assess the initiation of the APP for specific initial TA or Ω_{ar} levels (see regressions in Fig. 4). In this regard, Fig. 6 illustrates the correlations of the curve-fitted coefficients (b) and (c) and their related entities of the modeled induction times and APP timespans (see Fig. 2). Under the present physicochemical conditions, the provided regressions could be utilized as conversion equations to estimate the TA development of a treated water mass based on an existing database or to convert observational data into mathematically expressible equations for predicting the future evolution.



Figure 6: Regressions describing the relationships between the coefficient (b) and the modeled induction time [A], as well as the coefficient (c) and the modeled APP timespan [B] for each approach. The shown regressions allow for the conversion of specifiable time-dependent characteristics of a runaway process to the coefficients of the presented inverse logistic function (Eq. (1)). Specified relationships should not be generalized and are only valid within the given conditions of each approach.



230

231 3.5 Empirical rate equations

232 Further implications about the reaction speed and the related timespan of the APP can be provided by empirical
 233 rate law equations. As an example, Fig. 7 demonstrates the relationship between the logarithm of TA-loss rates
 234 normalized by surface area and aragonite saturation states for the unfiltered neq approach (see Fig. S4 and S5 for
 235 details on filtered approaches), for treatments that entered the accelerated precipitation phase. Throughout all
 236 experiments $\log(R)$ TA-loss rates correlate with the $\log(\Omega_{ar}-1)$, expressing the characteristic relationship for
 237 carbonate formation (see Morse et al., 2007; Mucci & Morse, 1983; Zhong & Mucci, 1989). The strong correlation
 238 of the linear regressions within each experiment enables the articulation of the empirical rate equations, such as
 239 Eq. (2): $R = k(\Omega_{ar} - 1)^n$. In this equation R represents the surface area normalized TA-loss rate, k the rate



constant and n the reaction order. The related values for n and $\log(k)$ derived from the linear regressions are provided in Tab. 3 (see Tab. S1 and S2 for filtered experiments), showing reasonable consistency in n and $\log(k)$ values within each of the three separate experiments. While some treatments, showing immediate $\text{Mg}(\text{OH})_2$ formation, slightly deviate, the other treatment levels displayed reaction orders (n) within a relatively narrow range of 2.45 to 2.73. In comparison, $\log(k)$ values ranged between 0.30-1.68, showcasing a higher variability.

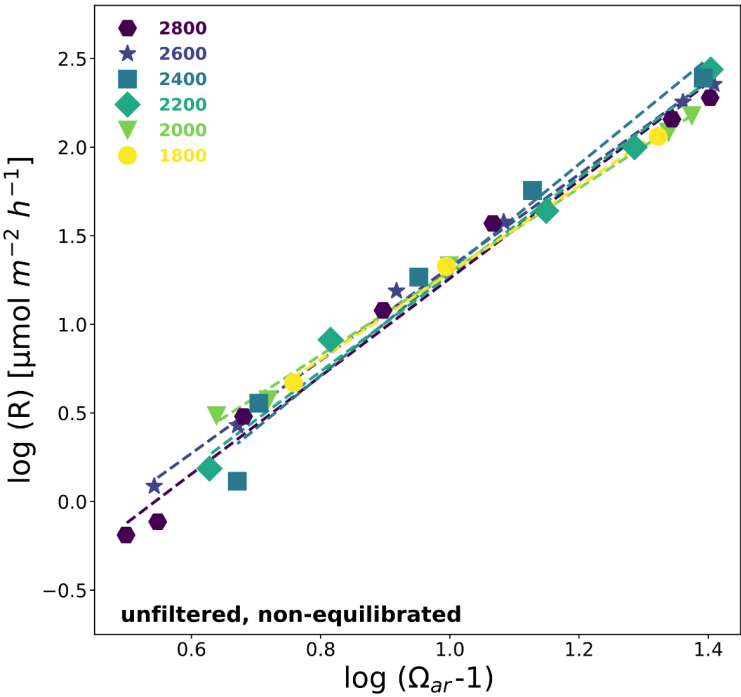


Figure 7: Carbonate precipitation kinetics for unfiltered neq treatments that entered the APP; see Tab. 3 for related regressions and rate equations.

Table 3: Overview of coefficients and regressions of empirical rate equations for unfiltered neq treatments, also see Fig. 7

Treatment	$\log(R) = n(\Omega_{ar} - 1) + \log(k)$			
ΔT_A	n	$\log(k)$	R^2	$\hat{\sigma}$
2800	2.76	-1.50	0.989	0.117
2600	2.62	-1.30	0.997	0.055
2400	2.98	-1.68	0.975	0.167
2200	2.73	-1.45	0.989	0.106
2000	2.35	-1.06	0.997	0.046
1800	2.45	-1.16	0.996	0.060
all	2.68	-1.39	0.985	0.106



250 **3.6 Evolution of particles and sinking speed**

251 To assess the impact of secondary precipitated particles during OAE approaches, precipitated materials from the
252 studies by Hartmann et al. (2023) and Suitner et al. (2024) were analyzed for shape, size, and sinking velocity. As
253 qualitatively depicted in the study of Suitner et al. (2024) (see Fig. 7 therein) the aragonite precipitates manifest
254 and evolve in a variety of forms and sizes, ranging from stem-like structures, followed by double-broccoli shapes
255 and ultimately forming closed spheres.

256 For this study the length and width distribution of 950 precipitated particles were determined by manual inspection
257 of four overview SEM images (see Fig. S1) from Gran Canaria samples (see Hartmann et al., 2023 for details;
258 analyzed treatment level: ΔTA_{2400} , filtered, neq, Temp. $\sim 23^{\circ}\text{C}$, Sal. ~ 36.5 , runtime 4 days) and the Raunefjorden,
259 Bergen (this study and Suitner et al., 2024, see Figs. 3 and 7 therein; analyzed treatment levels: ΔTA_{2800} and
260 ΔTA_{2600} , Temp. $\sim 11^{\circ}\text{C}$, Sal. 32.6, runtime 25 days – highest unfiltered neq treatments). Results of this evaluation
261 are provided in Fig. S6. Length and width distributions of the formed particles follow distinct ratios, allowing the
262 definition of three categories: **1. Stems** (<0.5), **2. Broccoli** ($0.5 < x < 0.9$) and **3. Spheres** (>0.9). Note that this method
263 also categorizes regularly shaped, multi-branched particles as spheres (see Fig. 8). Precipitates from the Gran
264 Canarian campaign primarily comprised well-developed broccoli and spherical-shaped particles, whereas the
265 samples from the Raunefjorden were characterized by less evolved stems and broccoli as the dominant
266 components. Although the runtime for the Gran Canarian sample was considerably shorter (4 days) in comparison
267 to the Raunefjorden (25 days), the $\sim 12^{\circ}\text{C}$ difference in temperature led to significantly higher precipitation rates
268 and more developed shapes. The analyzed Raunefjorden samples originate from the same experiment and differ
269 only in the initially added TA-level of $200\text{ }\mu\text{mol kg}^{-1}$. Even this minor difference in TA addition resulted in the
270 presence of more evolved shapes in the higher treatment.

271 Based on the distributions of equivalent spherical diameters (ESD), the sinking velocities of the precipitated
272 materials were calculated to identify their hypothetical sinking velocities. To facilitate this calculation, the
273 densities of the aragonite precipitates were determined by actual sinking velocity measurements of the same
274 materials, providing densities of 1.54 to 3.18 g cm^{-3} in an ESD range of 12 - $50\text{ }\mu\text{m}$. The discrepancy with the
275 density of aragonite ($\sim 2.95\text{ g cm}^{-3}$) may result from an overestimation of particle sizes in the calculation method,
276 which relies on an inversion of Stokes' Law for the terminal sinking velocity of perfect spheres. However, most
277 particles are not spherical and contain numerous cavities within their structure, which likely contributes to an
278 underestimation of particle densities. Therefore, Fig. 8 features a range of sinking velocities of the counted
279 precipitates in dependence to a variable density, supported by ESD distributions and ranges for different types of
280 precipitated particles. Measured sinking velocities for precipitated particles within the aforementioned density
281 range varied from $\sim 5\text{ m d}^{-1}$ ($14\text{ }\mu\text{m}$ particle) to $\sim 47\text{ m d}^{-1}$ ($41\text{ }\mu\text{m}$ particle). Recorded particles in the ESD range of
282 50 - $180\text{ }\mu\text{m}$ were not included in the calculations, as they were not observed within the same filter material that
283 was analyzed by visual inspection, yielding densities of 1.1 - 1.3 g cm^{-3} . Discrepancies between measured and
284 calculated values may reflect aggregation effects for very high values and the technical limitations of the utilized
285 FlowCam to track particles smaller than $3\text{ }\mu\text{m}$ (Bach et al., 2012).

286 Derived from the calculated sinking velocities, the residence times within the upper 200 m of the water column
287 were determined. Accordingly, early precipitated stages, such as stems ($<10\text{ }\mu\text{m}$), could remain for a few months
288 within the upper ocean layer, providing potential additional surfaces for an ongoing heterogeneous precipitation
289 if a continuous local alkalization is applied. In contrast, precipitates $>30\text{ }\mu\text{m}$ would descend within days to deeper
290 ocean layers, not affecting the precipitation behavior of continuous surface alkalization attempts. Notice that



291 sinking velocities are temperature and salinity dependent, and therefore would vary under different environmental
 292 conditions (see Fig. S7).

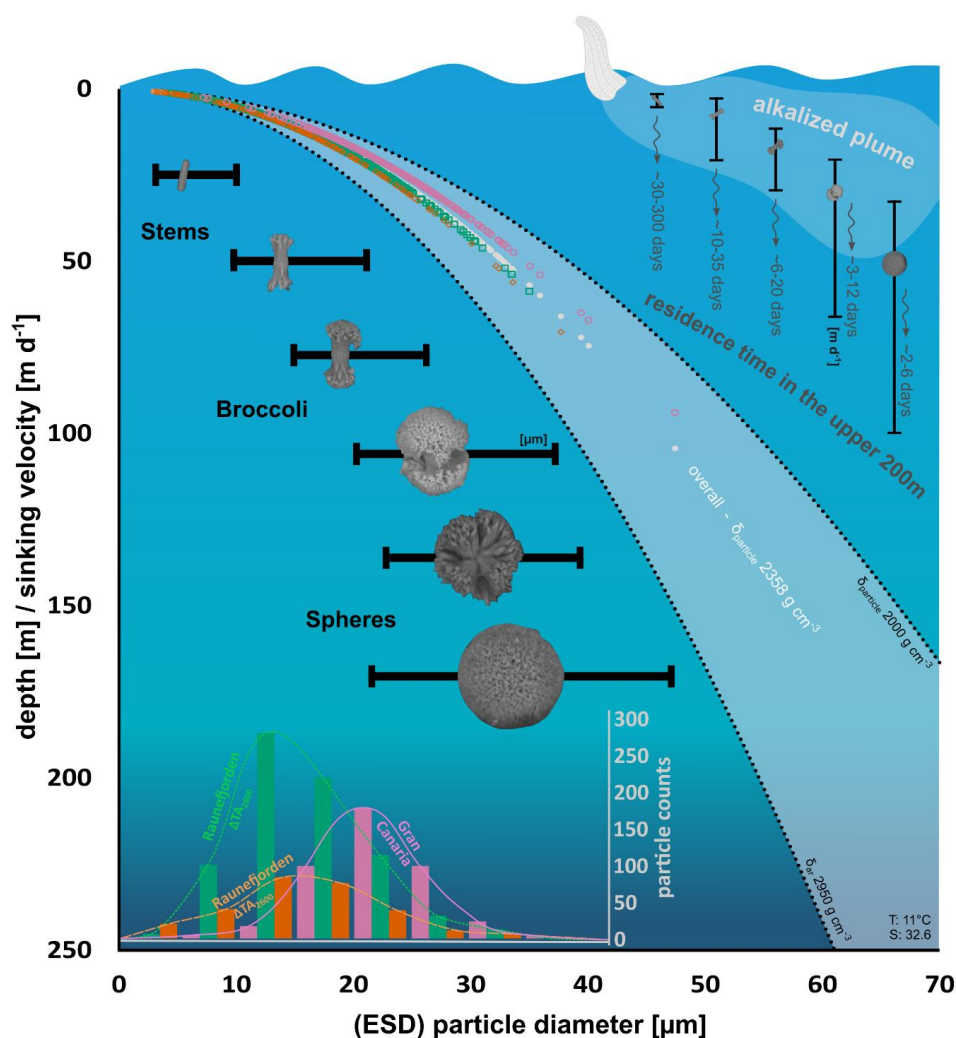


Figure 8: Overview of grain size distributions of precipitated particles, expressed as ESD (equivalent spherical diameter) in μm (black bars) and particle counts in size fractions steps of $5 \mu\text{m}$ (histogram, also see Fig. S6); calculated sinking velocities of particles (hollow markers) as a function of ESD for each treatment (green squares: neq unfiltered ΔTA_{2800} – Raunefjorden, Bergen; orange diamonds: neq unfiltered ΔTA_{2600} Raunefjorden, Bergen; pink circles: neq filtered ΔTA_{2400} Gran Canaria). The mean time range for average particles of their class (stems, broccoli, spheres) to sink below the mixed layer depth (assumed to be 200m), neglecting particle growth processes.

293



294 **4 Discussion**

295 **4.1 General findings**

296 By analyzing the experimental datasets provided by Suitner et al. (2024), this study demonstrates that the process
297 of alkalinity loss during runaway carbonate precipitation follows quantifiable relationships. For the present study,
298 the compiled concepts allowed the description of the principles guiding the entire runaway process. The obtained
299 capability to predict TA-stability ranges, in terms of time and magnitude, might help preventing secondary mineral
300 formation, thereby optimizing the assessments for OAE application scenarios. Furthermore, the simplicity of the
301 logistic curve fit model, along with the demonstration that the carbonate precipitation follows simple rate law
302 equations (see Morse et al., 2007; Mucci & Morse, 1983; Zhong & Mucci, 1989), might facilitate the
303 straightforward integration of these fundamental mechanisms into ocean models like the studies by He & Tyka
304 (2023), Ou et al. (2025), Schwinger et al. (2024), Wang et al. (2022) or Zhou et al. (2024).

305

306 **4.2 Nucleation and onset of accelerated precipitation phase**

307 Previous studies examining the evolution of the runaway precipitation process in the context of OAE (Hartmann
308 et al., 2023; Moras et al., 2022, 2024; Suitner et al., 2024) observed and described considerable periods with stable
309 TA levels before the onset of the APP (e.g. see Fig. 1 modified after Suitner et al., 2024), depending on the
310 alkalinity and DIC levels.

311 In theory, even at natural background supersaturation levels in the ocean, (pseudo-)homogeneous precipitation is
312 expected to occur at very slow rates, on timescales of thousands of years (Pytkowicz, 1965, 1973). Regardless, the
313 nucleation and precipitation processes in ocean waters are suppressed by inhibitory species like Mg^{2+} (Berner,
314 1975; Pan et al., 2021; Pokrovsky, 1998), phosphate- (Burton & Walter, 1990) or dissolved organic matter (Chave
315 & Suess, 1970; Kellock et al., 2022; Moras et al., 2024). Naturally occurring precipitation events in the ocean are
316 associated with unique occurrences such as flash floods (Wurgaft et al., 2016, 2021) or whittings (Broecker &
317 Takahashi, 1966; Bustos-Serrano et al., 2009; Morse et al., 2003), providing high degrees of (re)suspended
318 sediments that catalyze a heterogeneous carbonate precipitation procedure.

319 To consider the persistent (pseudo-)homogeneous precipitation within typical natural seawater supersaturation
320 ranges, the terminology concerning specific stability ranges of TA or timeframes for the onset of secondary
321 carbonate formation should be refined. However, within typical observation times in the Earth system, the
322 precipitation of secondary calcium carbonate in particle-free seawater solutions is expected to be suppressed to
323 Ω_{ar} values of approximately 11.3 or below (derived from Eq. (4) in Marion et al. (2009), based on data by Morse
324 & He (1993) and Morse et al. (2007)).

325 Nevertheless, even a $0.2\mu m$ -filtered natural seawater contains around $\sim 10^9$ particles per ml in the size range of 5-
326 120 nm, already offering a total surface area of around $8 m^2$ per m^3 (cf. Wells & Goldberg, 1992), potentially
327 acting as a catalyst to initiate carbonate precipitation in alkalinity treated seawater. In the presence of surfaces for
328 pseudo-homogeneous/ heterogeneous such as suspended sediments, colloids, organic matter or the introduced
329 solid alkanization substrates, Moras et al. (2022) reported an Ω_{ar} threshold of $\sim 5-7$ for the observable onset of
330 carbonate formation for the given runtime of the experiment. Potentially, the colloidal structure of $Mg(OH)_2$
331 precipitates (see Badjatya et al., 2022), typically formed above pH values of ~ 10.5 as a consequence of alkalinity
332 addition (cf. Eisaman et al., 2023; Haas, 1916; Kapp, 1928; Suitner et al., 2024; Varliero et al., 2024) could serve



the same purpose and lower the threshold for carbonate precipitation. However, the redissolution of the formed $\text{Mg}(\text{OH})_2$ through the mixing and dilution processes, as described by Ringham et al. (2024), may inhibit this effect and would also allow much higher short-term pH and TA concentrations around an alkalinity injection site when using liquid stock solutions.

To characterize the transition from a state with negligible shifts in carbonate chemistry towards a phase primarily driven by carbonate formation (cf. Suitner et al., 2024), a practicable criterion of a $40 \mu\text{mol kg}^{-1} \text{d}^{-1}$ TA-loss was set to determine the start of the intensified precipitation stage (see Figs. 4 and 5). This criterion was also used to describe the induction time, which is the period before a measurable onset of secondary carbonate formation can be detected (Fig. 4). Since the induction time includes a fundamental uncertainty, it does not reflect an intrinsic property of the treated solution itself and relies on the detection capability of the experimental setup (Söhnel & Mullin, 1988) and might be chosen differently in future work (see Fig. S9 for varying criteria). While the selected criterion already depicts relatively high loss rates, it enables detectable changes, distinguishable from measurement uncertainties or natural variabilities. The overall emerging patterns related to the onset and duration of the APP nevertheless remained relatively consistent across different tested threshold values.

4.3 Predictability of the runaway process

The consistent patterns during the alkalinity loss within all three experimental setups allowed the introduction of continuous and differentiable functions for each treatment level, enabling further analysis to examine relevant factors guiding the runaway process. Fuhr et al. (2022) utilized a comparable inverted logistic function to model the process of secondary carbonate formation during olivine dissolution experiments in seawater. However, the model was not consistently applied to describe a runaway carbonate precipitation process nor used as a general predictive model to determine the stability ranges of the added alkalinity in OAE approaches.

The characteristics of the logistic function applied in this study, facilitate the conversion of both empirically determined and hypothetical parameters, such as induction time, duration of the APP (Fig. 5), or the initial and final TA levels before and after the runaway process. The applicability of kinetic rate equations, combined with the ability to quantify the precipitation process, enables a description and prediction of the temporal evolution of the carbonate formation. This may facilitate the integration of the alkalinity depletion procedure into various predictive modeling approaches. Although these statements currently apply only under the tested environmental conditions, they nonetheless suggest the general capability to assess a framework for guiding time and TA level ranges in OAE approaches. Since the logistic model is based on experimental data from bottle experiments, processes such as the removal of surface area due to the sinking of precipitated carbonate particles were not accounted for - see section 4.6 for an approach to address this topic.

Under specified temperature and salinity conditions, as well as predefined TA/DIC levels after OAE treatment and an estimated final Ω_{ar} after the precipitation process stopped (typically ~ 1.5 - 5.0 , see Fuhr et al., 2022; Hartmann et al., 2023; Moras et al., 2022; Pan et al., 2021; Suitner et al., 2024), the resulting total TA-loss can be computed. This calculation follows the condition that the alkalinity loss reflects the ideal 2:1 TA:DIC ratio during carbonate mineral precipitation in seawater (Zeebe & Wolf-Gladrow, 2001). Given these assumptions, upper and lower limits of the logistic function (coefficients **(a)** and **(d)**, Eq. (1)) can be determined. To characterize measures such as induction time (coefficient **(b)**) and the duration of the APP (coefficient **(c)**), it is necessary to acquire empirical data that account for the specific conditions of the deployment area. These data could either be provided by actual experiments or model predictions, based on a comprehensive database which accounts for broad ranges of TA,



374 DIC, temperature, salinity, and practical available surface area, as well as inhibitory factors or potential effects of
375 biota. To validate the predicted precipitation behavior, additional gradient experiments need to be conducted to
376 better understand the geochemical reaction pathways.

377

378 **4.4 Empirical rate equations using Ω_{ar} and particle surface area during APP**

379 After passing the induction time to start the detectable carbonate formation process by (pseudo-/)homogeneous
380 precipitation and overcoming the delaying inhibition effects (Marion et al., 2009; Morse & He, 1993; Schulz et
381 al., 2023), the triggered heterogeneous precipitation can be described by basic empirical rate equations (Fig. 7, S4
382 and S5). These equations demonstrate the fundamental role of Ω_{ar} as a guiding factor for the precipitation process.
383 The kinetics of carbonate formation remained relatively consistent across all treatment levels within each
384 experimental approach (see Tabs. 3, S1 and S2). The observed consistent correlations between saturation states
385 and surface area normalized precipitation rates indicate that the runaway carbonate formation processes during the
386 present incubations followed the known kinetics of heterogeneous carbonate formation in seawater (cf. Morse et
387 al., 2007; Zhong & Mucci, 1989).

388 Fig. 9 illustrates the role of Ω_{ar} saturation states and generated surface area in guiding the alkalinity loss rates
389 during the precipitation process. The black graph represents the curve fit of TA-loss rates of the unfiltered neq
390 ΔTA_{2000} approach; the experimentally determined rates are indicated by black triangles (cf. Fig. 3c). Assuming
391 that the entire lost alkalinity was transformed into aragonite precipitates with a surface area of $2.283 \text{ m}^2 \text{ g}^{-1}$ (see
392 chapter 2.3), the total generated particle surface area (PSA) could be determined (red dotted graph). The overall
393 expected TA-loss rate per m^2 (brown dashed graph) was obtained by utilizing the empirical logistic curve fit for
394 the temporal evolution of Ω_{ar} (Fig. 3b), normalizing it to 1 m^2 surface area, and inserting it into the rate equation
395 (Eq. (4)). Given that the system initially exhibits a negligible degree of PSA, the relatively high precipitation
396 potential by the Ω_{ar} saturation state does not result in a measurable TA-loss rate. Following the presented concept,
397 the consistently high Ω_{ar} values led to a continuous (pseudo-/)homogeneous precipitation during the induction
398 time, thus causing a rise in PSA until the system shifts to heterogeneous precipitation, and ultimately resulting in
399 a detectable exponential runaway process. The interplay of precipitation potential by Ω_{ar} and the practical available
400 surface area could therefore be determined as the primary factors guiding the actual observed TA-loss rates.

401 Within the uncertainties of the applied calculation steps and methods, the practical TA-loss rate could simply be
402 described as the product of these two factors (also see Fig. S8 for other treatments). For comparison, the blue data
403 points in Fig. 9 represent the calculated theoretical loss rates at each sampling day, by inserting the experimentally
404 determined Ω_{ar} and PSA values into the related empirical rate equation for ΔTA_{2000} (see Tab. 3). As this equation
405 does not account for any inhibitory factors, the resulting rates exhibit a slight positive bias compared to the
406 observed values.

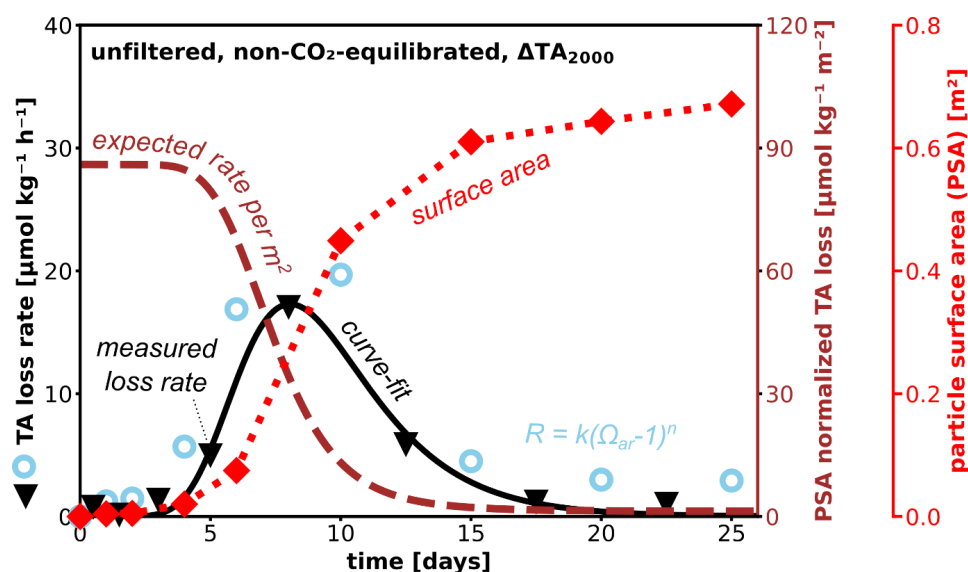


Figure 9: Conceptual figure, illustrating the interplay of Ω_{ar} and particle surface area guiding the TA-loss rate evolution (dashed, dark red). After TA injection high Ω_{ar} values provide a high potential for the formation of carbonates by heterogeneous precipitation. In the absence of existing particle surface area (red dotted), (pseudo-)homogenous precipitation would dominate the period until the start of the APP and the resulting runaway precipitation process. Observed TA-loss rates (black triangles) are therefore a combination of the available practical surface area and the precipitation potential by Ω_{ar} oversaturation. While the potential to precipitate carbonates decreases with progressive precipitation, additional surface area is generated. The symmetry of the TA-loss rate can be mathematically described with good approximation using only these two factors. Understanding how long particles remain in a critical zone to maintain a full-grown runaway process is therefore relevant for future considerations. Hollow light-blue markers provide the output of the related empirical rate equations for each sampling day. The shown TA and loss rate data are taken from the empirical data sets for the neq unfiltered ΔTA_{2000} approach, see Fig. S4 for other treatments levels.

407

408 4.5 Could a runaway process be triggered in an open world context?

409 Mixing with untreated water around an injection point may lead to an efficient dilution below non-critical alkalinity
 410 levels within seconds to minutes. Such a process would effectively prevent alkalinity leakage, as described in this
 411 study, which assumes that the formed particles act as catalysts for future precipitation. This is supported by findings
 412 from a mesocosm experiment and corresponding side experiments, where the presence of additional suspended
 413 aragonite particles accelerated the alkalinity loss (Paul et al., 2024). In contrast, fresh seawater enhanced to the
 414 same TA-levels did not show any alkalinity loss within 10 days in their experiments. These observations indicate
 415 that free-floating particles in the water column can accelerate heterogeneous precipitation in a runaway style.
 416 Precipitation events can be triggered naturally without additional treatment, especially for locations with already
 417 relatively high Ω_{ar} background levels, for example, due to high evaporation rates (Bialik et al., 2022) or high
 418 degrees of (re)suspended sediments present on carbonate platforms (Broecker & Takahashi, 1966; Bustos-Serrano
 419 et al., 2009; Morse et al., 2003), or close to river mouths (Wurgaft et al., 2016, 2021) providing additional PSA to
 420 catalyze precipitation events. Under inappropriate alkalinity deployment circumstances, secondary mineral
 421 formation might be triggered locally around injection sites, within short timescales. Moras et al. (2022) suggested



that visible APP starts around Ω_{ar} of 5, which translates for the mostly particle-free water of the Raunefjorden into $\Delta TA \sim 245 \mu\text{mol kg}^{-1}$ applying a neq OAE approach and $\Delta TA \sim 580 \mu\text{mol kg}^{-1}$ for an eq OAE approach. The induction time before the APP begins can be estimated using Equation (5), based on the specified TA-loss criterion of $40 \mu\text{mol kg}^{-1} \text{ d}^{-1}$. For these configurations, the projected induction times would be 1074 days and 143 days, respectively. However, the predicted induction times lie far outside the calibration ranges specified in this study and may therefore be inaccurate. Nevertheless, since these projected APP induction times are also within the suggested residence times of treated water in the upper ocean layers, it is necessary to conduct studies lasting at least for the projected timespans, depending on the local environmental conditions. Significantly shorter induction times were identified for subtropical conditions (Temp. $\sim 23^\circ\text{C}$, Sal. ~ 36 psu, TA $\sim 2400 \mu\text{mol kg}^{-1}$). Hartmann et al. (2023) described an onset of the precipitation after just 4 days for a $50 \mu\text{m}$ filtered neq incubation with initial values of $1050 \mu\text{mol kg}^{-1}$ for ΔTA and ~ 15 for Ω_{ar} . Within the same setting, Paul et al. (2024) observed aragonite formation for a CO_2 equilibrated setup with $\Delta TA \sim 2300 \mu\text{mol kg}^{-1}$ and $\Omega_{ar} 9.74 \pm 0.15$ in mesocosms after 21 days.

4.6 Consequence of sinking particles removing surface area for carbonate formation

Because the TA-loss rate is proportional to the surface area of particles (Eq. (4)), removal of particles due to sinking processes or dilution with untreated water would result in slower precipitation rates. Small, formed particles may remain in the upper layer for several months (Fig. 8), while medium-sized particles may leave the treated water within a couple of days, depending on temperature and salinity conditions (Figs. 8 and S7). Particles larger than $15 \mu\text{m}$ are expected to sink within one day under the environmental conditions of the Raunefjorden. If those particles were removed by sinking while they were still growing, it can be estimated that approximately 30-40% of the available surface area would be removed from the upper 10 m of the water column within one day (also see SI). This would decrease the precipitation rate accordingly as surface area and formation rates are linearly proportional. Potential aggregation would increase the sinking speed and was not considered in this model calculation but may be relevant in other settings. In general, the abundance and sinking of particles need to be addressed if the stability or loss of is to be assessed with a high level of confidence. Efficient dilution of the treated water parcels could therefore significantly reduce ongoing precipitation, especially if the onset of the APP is initiated within the first few seconds. For example, this could be the case in the wake of a ship, in OAE applications utilizing existing marine traffic to distribute alkalinity throughout the world's oceans (Caserini et al., 2021). However, particle-based alkalization approaches would nevertheless temporarily introduce additional surface area until its complete dissolution, and may cause the shift into the APP (Hartmann et al., 2023).



454 **5 Conclusion**

455 Alkalinity leakage due to oversaturation sets a limit to the efficiency of OAE approaches. So far, the drivers of the
456 process could not be quantified, preventing the implementation of TA-loss terms in applicability assessments for
457 OAE. An induced runaway process follows predictable patterns that can be modeled using available surface area
458 and aragonite oversaturation, identified as the main factors for the given environmental settings.
459 However, it is expected that parameterizations will systematically change along temperature and salinity gradients,
460 as well as with naturally occurring variations in particle abundance and quality. The determination of their impact
461 was not within the scope of this work, instead this study aimed to provide a framework for how such needed
462 parameterization can be achieved. Achieving a predictability of the induced TA-loss on a global scale would allow
463 the identification of suitable locations for OAE or optimizing applications. Therefore, further research across
464 salinity and temperature gradients would also enhance the predictive capabilities of ocean models. Runaway TA-
465 loss processes, as described in this study, would be significantly altered under natural conditions by dilution and
466 particle export processes. If sinking of particles and dilution with untreated water are considered, the limitations
467 of laboratory bottle experiments become evident. Nevertheless, they contribute valuable parameterizations for
468 model development. Field experiments are necessary to evaluate the validity of the presented theoretical model
469 framework with respect to dilution and particle sinking processes.
470



471 **Data availability**

472 All datasets will be made available at the time of publication.

473 **Author contributions**

474 The idea for this work was conceived by NS, with contributions by JH and SV. NS, SV and PS performed the
475 surface area- and sinking velocity/density measurements. NS interpreted the data with help from all co-authors.
476 NS and JH wrote the text with contributions from all co-authors.

477 **Acknowledgements**

478 Peggy Bartsch (UHH), Carl Lim (UHH) and Julieta Schneider (GEOMAR) are thanked for supporting the
479 preparation and execution of the experiments.

480 **Financial support**

481 This research has been supported by the German Federal Ministry of Education and Research through the
482 CDRmare projects RETAKE-1: grant no. 03F0895F and RETAKE-2: grant no. 03F0965F; Horizon 2020
483 (OceanNETs; grant no. 869357); the Deutsche Forschungsgemeinschaft (grant no. 390683824), under Germany's
484 Excellence Strategy (EXC 2037, "CLICCS"; grant no. 390683824) contribution to the Center for Earth System
485 Research and Sustainability (CEN) of Universität Hamburg, as well as the Ocean Alkalinity Enhancement (OAE)
486 R&D Program funded by the Carbon to Sea Initiative.

487 **Competing interests**

488 JHA is consulting the Planetears GmbH. The contact authors have declared that all other authors have no
489 competing interests.



References

- Bach, L. T., Riebesell, U., Sett, S., Febiri, S., Rzepka, P., & Schulz, K. G. (2012). An approach for particle sinking velocity measurements in the 3–400 µm size range and considerations on the effect of temperature on sinking rates. *Marine Biology*, 159(8), 1853–1864. <https://doi.org/10.1007/s00227-012-1945-2>
- Badjatya, P., Akca, A. H., Fraga Alvarez, D. V., Chang, B., Ma, S., Pang, X., Wang, E., van Hinsberg, Q., Esposito, D. V., & Kawashima, S. (2022). Carbon-negative cement manufacturing from seawater-derived magnesium feedstocks. *Proc Natl Acad Sci U S A*, 119(34), e2114680119. <https://doi.org/https://doi.org/10.1073/pnas.2114680119>
- Berner, R. A. (1975). The role of magnesium in the crystal growth of calcite and aragonite from sea water. *Geochimica et Cosmochimica Acta*, 39(4), 489–504. [https://doi.org/https://doi.org/10.1016/0016-7037\(75\)90102-7](https://doi.org/https://doi.org/10.1016/0016-7037(75)90102-7)
- Bialik, O. M., Sisma-Ventura, G., Vogt-Vincent, N., Silverman, J., & Katz, T. (2022). Role of oceanic abiotic carbonate precipitation in future atmospheric CO₂ regulation. *Sci Rep*, 12(1), 15970. <https://doi.org/https://doi.org/10.1038/s41598-022-20446-7>
- Broecker, W. S., & Takahashi, T. (1966). Calcium carbonate precipitation on the Bahama Banks. *Journal of Geophysical Research*, 71(6), 1575–1602. <https://doi.org/https://doi.org/10.1029/JZ071i006p01575>
- Brunauer, S., Emmett, P. H., & Teller, E. (1938). Adsorption of gases in multimolecular layers. *Journal of the American chemical society*, 60(2), 309–319.
- Burton, E. A., & Walter, L. M. (1990). The role of pH in phosphate inhibition of calcite and aragonite precipitation rates in seawater. *Geochimica et Cosmochimica Acta*, 54(3), 797–808. [https://doi.org/https://doi.org/10.1016/0016-7037\(90\)90374-T](https://doi.org/https://doi.org/10.1016/0016-7037(90)90374-T)
- Bustos-Serrano, H., Morse, J. W., & Millero, F. J. (2009). The formation of whittings on the Little Bahama Bank. *Marine Chemistry*, 113(1–2), 1–8. <https://doi.org/https://doi.org/10.1016/j.marchem.2008.10.006>
- Caserini, S., Pagano, D., Campo, F., Abbà, A., De Marco, S., Righi, D., Renforth, P., & Grosso, M. (2021). Potential of Maritime Transport for Ocean Liming and Atmospheric CO₂ Removal. *Frontiers in Climate*, 3. <https://doi.org/https://doi.org/10.3389/fclim.2021.575900>
- Chave, K. E., & Suess, E. (1970). Calcium Carbonate Saturation in Seawater: Effects of Dissolved Organic Matter. *Limnology and Oceanography*, 15(4), 633–637. <https://doi.org/https://doi.org/10.4319/lo.1970.15.4.0633>
- Eisaman, M., Geilert, S., Renforth, P., Bastianini, L., Campbell, J., Dale, A., Foteinis, S., Grasse, P., Hawrot, O., & Löscher, C. (2023). Chapter 3: Assessing the technical aspects of OAE approaches. *State of the Planet Discussions*, 2023, 1–52. <https://doi.org/https://doi.org/10.5194/sp-2-oae2023-3-2023>
- Faucher, G., Haunost, M., Paul, A. J., Tietz, A. U. C., & Riebesell, U. (2024). Growth response of *Emiliania huxleyi* to ocean alkalinity enhancement. *EGUsphere*, 2024, 1–17. <https://doi.org/10.5194/egusphere-2024-2201>
- Ferderer, A., Chase, Z., Kennedy, F., Schulz, K. G., & Bach, L. T. (2022). Assessing the influence of ocean alkalinity enhancement on a coastal phytoplankton community. *Biogeosciences*, 19(23), 5375–5399. <https://doi.org/10.5194/bg-19-5375-2022>
- Fuhr, M., Geilert, S., Schmidt, M., Liebetrau, V., Vogt, C., Ledwig, B., & Wallmann, K. (2022). Kinetics of Olivine Weathering in Seawater: An Experimental Study. *Frontiers in Climate*, 4. <https://doi.org/https://doi.org/10.3389/fclim.2022.831587>
- Fuss, S., Lamb, W. F., Callaghan, M. W., Hilaire, J., Creutzig, F., Amann, T., Beringer, T., de Oliveira Garcia, W., Hartmann, J., Khanna, T., Luderer, G., Nemet, G. F., Rogelj, J., Smith, P., Vicente, J. L. V., Wilcox, J., del Mar Zamora Dominguez, M., & Minx, J. C. (2018). Negative emissions—Part 2: Costs, potentials and side effects. *Environmental Research Letters*, 13(6). <https://doi.org/10.1088/1748-9326/aabf9f>
- Gately, J. A., Kim, S. M., Jin, B., Brzezinski, M. A., & Iglesias-Rodriguez, M. D. (2023). Coccolithophores and diatoms resilient to ocean alkalinity enhancement: A glimpse of hope? *Science Advances*, 9(24), eadg6066. <https://doi.org/10.1126/sciadv.adg6066>
- Goldenberg, S. U., Riebesell, U., Brüggemann, D., Börner, G., Sswat, M., Folkvord, A., Couret, M., Spjelkavik, S., Sánchez, N., Jaspers, C., & Moyano, M. (2024). Early life stages of fish under ocean alkalinity enhancement in coastal plankton communities. *Biogeosciences*, 21(20), 4521–4532. <https://doi.org/10.5194/bg-21-4521-2024>
- Haas, A. R. (1916). The Effect of the Addition of Alkali to Sea Water Upon the Hydrogen Ion Concentration. *Journal of Biological Chemistry*, 26(2), 515–517. [https://doi.org/https://doi.org/10.1016/s0021-9258\(18\)7433-6](https://doi.org/https://doi.org/10.1016/s0021-9258(18)7433-6)
- Hartmann, J., Suitsner, N., Lim, C., Schneider, J., Marín-Samper, L., Aristegui, J., Renforth, P., Taucher, J., & Riebesell, U. (2023). Stability of alkalinity in ocean alkalinity enhancement (OAE) approaches – consequences for durability of CO₂ storage. *Biogeosciences*, 20(4), 781–802. <https://doi.org/https://doi.org/10.5194/bg-20-781-2023>



- 548 Hartmann, J., West, A. J., Renforth, P., Köhler, P., De La Rocha, C. L., Wolf-Gladrow, D. A., Dürr, H. H., &
549 Scheffran, J. (2013). Enhanced chemical weathering as a geoengineering strategy to reduce atmospheric
550 carbon dioxide, supply nutrients, and mitigate ocean acidification. *Reviews of Geophysics*, 51(2), 113-
551 149. <https://doi.org/https://doi.org/10.1002/rog.20004>
- 552 Harvey, L. D. D. (2008). Mitigating the atmospheric CO₂ increase and ocean acidification by adding limestone
553 powder to upwelling regions. *Journal of Geophysical Research: Oceans*, 113(C4).
554 <https://doi.org/10.1029/2007jc004373>
- 555 He, J., & Tyka, M. D. (2023). Limits and CO₂ equilibration of near-coast alkalinity enhancement. *Biogeosciences*,
556 20(1), 27-43. <https://doi.org/https://doi.org/10.5194/bg-20-27-2023>
- 557 Ilyina, T., Six, K. D., Segschneider, J., Maier-Reimer, E., Li, H., & Núñez-Riboni, I. (2013). Global ocean
558 biogeochemistry model HAMOC: Model architecture and performance as component of the MPI-Earth
559 system model in different CMIP5 experimental realizations. *Journal of Advances in Modeling Earth*
560 *Systems*, 5(2), 287–315. <https://doi.org/https://doi.org/10.1029/2012ms000178>
- 561 Inskeep, W. P., & Bloom, P. R. (1985). An evaluation of rate equations for calcite precipitation kinetics at pCO₂
562 less than 0.01 atm and pH greater than 8. *Geochimica et Cosmochimica Acta*, 49(10), 2165-2180.
563 [https://doi.org/https://doi.org/10.1016/0016-7037\(85\)90074-2](https://doi.org/https://doi.org/10.1016/0016-7037(85)90074-2)
- 564 IPCC. (2023). Technical Summary. In *Climate Change 2021 – The Physical Science Basis* (pp. 35-144).
565 <https://doi.org/10.1017/9781009157896.002>
- 566 Iyer, G., Hultman, N., Eom, J., McJeon, H., Patel, P., & Clarke, L. (2015). Diffusion of low-carbon technologies
567 and the feasibility of long-term climate targets. *Technological Forecasting and Social Change*, 90, 103-
568 118. <https://doi.org/10.1016/j.techfore.2013.08.025>
- 569 Kapp, E. M. (1928). The precipitation of calcium and magnesium from sea water by sodium hydroxide. *The*
570 *Biological Bulletin*, 55(6), 453-458.
- 571 Kellock, C., Castillo Alvarez, M. C., Finch, A., Penkman, K., Kroger, R., Clog, M., & Allison, N. (2022).
572 Optimising a method for aragonite precipitation in simulated biogenic calcification media. *PLoS One*,
573 17(12), e0278627. <https://doi.org/https://doi.org/10.1371/journal.pone.0278627>
- 574 Kheshgi, H. S. (1995). Sequestering atmospheric carbon dioxide by increasing ocean alkalinity. *Energy*, 20(9),
575 915-922. [https://doi.org/https://doi.org/10.1016/0360-5442\(95\)00035-F](https://doi.org/https://doi.org/10.1016/0360-5442(95)00035-F)
- 576 Marín-Samper, L., Arístegui, J., Hernández-Hernández, N., Ortiz, J., Archer, S. D., Ludwig, A., & Riebesell, U.
577 (2024). Assessing the impact of CO₂-equilibrated ocean alkalinity enhancement on microbial metabolic
578 rates in an oligotrophic system. *Biogeosciences*, 21(11), 2859-2876. <https://doi.org/10.5194/bg-21-2859-2024>
- 579 Marion, G., Millero, F., & Feistel, R. (2009). Precipitation of solid phase calcium carbonates and their effect on
580 application of seawater S A–T–P models. *Ocean science*, 5(3), 285-291.
581 <https://doi.org/https://doi.org/10.5194/os-5-285-2009>
- 582 Minx, J. C., Lamb, W. F., Callaghan, M. W., Fuss, S., Hilaire, J., Creutzig, F., Amann, T., Beringer, T., de Oliveira
583 Garcia, W., Hartmann, J., Khanna, T., Lenzi, D., Luderer, G., Nemet, G. F., Rogelj, J., Smith, P., Vicente
584 Vicente, J. L., Wilcox, J., & del Mar Zamora Dominguez, M. (2018). Negative emissions—Part 1:
585 Research landscape and synthesis. *Environmental Research Letters*, 13(6). <https://doi.org/10.1088/1748-9326/aabf9b>
- 586 Moras, C. A., Bach, L. T., Cyronak, T., Joannes-Boyau, R., & Schulz, K. G. (2022). Ocean alkalinity enhancement
587 – avoiding runaway CaCO₃ precipitation during quick and hydrated lime dissolution. *Biogeosciences*,
588 19(15), 3537-3557. <https://doi.org/https://doi.org/10.5194/bg-19-3537-2022>
- 589 Moras, C. A., Cyronak, T., Bach, L. T., Joannes-Boyau, R., & Schulz, K. G. (2024). Effects of grain size and
590 seawater salinity on magnesium hydroxide dissolution and secondary calcium carbonate precipitation
591 kinetics: implications for ocean alkalinity enhancement. *Biogeosciences*, 21(14), 3463-3475.
592 <https://doi.org/10.5194/bg-21-3463-2024>
- 593 Morse, J. W., Arvidson, R. S., & Lüttge, A. (2007). Calcium carbonate formation and dissolution. *Chemical*
594 *reviews*, 107(2), 342-381. <https://doi.org/https://doi.org/10.1021/cr050358j>
- 595 Morse, J. W., Gledhill, D. K., & Millero, F. J. (2003). CaCO₃ precipitation kinetics in waters from the great Bahama
596 bank. *Geochimica et Cosmochimica Acta*, 67(15), 2819-2826.
597 [https://doi.org/https://doi.org/10.1016/s0016-7037\(03\)00103-0](https://doi.org/https://doi.org/10.1016/s0016-7037(03)00103-0)
- 598 Morse, J. W., & He, S. (1993). Influences of T, S and PCO₂ on the pseudo-homogeneous precipitation of CaCO₃
599 from seawater: implications for whiting formation. *Marine Chemistry*, 41(4), 291-297.
600 [https://doi.org/https://doi.org/10.1016/0304-4203\(93\)90261-L](https://doi.org/https://doi.org/10.1016/0304-4203(93)90261-L)
- 601 Mucci, A., & Morse, J. W. (1983). The incorporation of Mg²⁺ and Sr²⁺ into calcite overgrowths: influences of
602 growth rate and solution composition. *Geochimica et Cosmochimica Acta*, 47(2), 217-233.
603 [https://doi.org/https://doi.org/10.1016/0016-7037\(83\)90135-7](https://doi.org/https://doi.org/10.1016/0016-7037(83)90135-7)
- 604 Oeschies, A., Bach, L. T., Rickaby, R. E. M., Satterfield, T., Webb, R., & Gattuso, J.-P. (2023). Climate targets,
605 carbon dioxide removal, and the potential role of ocean alkalinity enhancement. *State of the Planet*, 2-
606 oae2023, 1-9. <https://doi.org/10.5194/sp-2-oae2023-1-2023>
- 607
- 608



- 609 Ou, Y., Xue, Z. G., & Hu, X. (2025). A numerical assessment of ocean alkalinity enhancement efficiency on a
610 river-dominated continental shelf – a case study in the northern Gulf of Mexico. *Environmental Research*
611 *Letters*. <https://doi.org/10.1088/1748-9326/adaa8b>
- 612 Pan, Y., Li, Y., Ma, Q., He, H., Wang, S., Sun, Z., Cai, W.-J., Dong, B., Di, Y., Fu, W., & Chen, C.-T. A. (2021).
613 The role of Mg²⁺ in inhibiting CaCO₃ precipitation from seawater. *Marine Chemistry*, 237.
614 <https://doi.org/https://doi.org/10.1016/j.marchem.2021.104036>
- 615 Paul, A. J., Haunost, M., Goldenberg, S. U., Hartmann, J., Sanchez, N. S., Schneider, J., Suitner, N., & Riebesell,
616 U. (2024). Ocean alkalinity enhancement in an open ocean ecosystem: Biogeochemical responses and
617 carbon storage durability. *EGUsphere*. <https://doi.org/https://doi.org/10.5194/egusphere-2024-417>
- 618 Pokrovsky, O. S. (1998). Precipitation of calcium and magnesium carbonates from homogeneous supersaturated
619 solutions. *Journal of Crystal Growth*, 186(1-2), 233-239. [https://doi.org/https://doi.org/10.1016/S0022-0248\(97\)00462-4](https://doi.org/https://doi.org/10.1016/S0022-0248(97)00462-4)
- 620 Pytkowicz, R. (1973). Calcium carbonate retention in supersaturated seawater. *American Journal of Science*,
621 273(6), 515-522. <https://doi.org/http://dx.doi.org/10.2475/ajs.273.6.515>
- 622 Pytkowicz, R. M. (1965). Rates of Inorganic Calcium Carbonate Nucleation. *The Journal of Geology*, 73(1), 196-
623 199. <https://doi.org/10.1086/627056>
- 624 Ramírez, L., Pozzo-Pirotta, L. J., Trebec, A., Manzanares-Vázquez, V., Díez, J. L., Arístegui, J., Riebesell, U.,
625 Archer, S. D., & Segovia, M. (2024). Ocean Alkalinity Enhancement (OAE) does not cause cellular stress
626 in a phytoplankton community of the sub-tropical Atlantic Ocean. *EGUsphere*, 2024, 1-34.
627 <https://doi.org/https://doi.org/10.5194/egusphere-2024-847>
- 628 Rau, G. H., & Caldeira, K. (1999). Enhanced carbonate dissolution as a means of sequestering carbon dioxide in
629 the ocean. *Energy Conversion and Management*, 40(17), 1803-1813. [https://doi.org/10.1016/S0196-8904\(99\)00071-0](https://doi.org/10.1016/S0196-8904(99)00071-0)
- 630 Renforth, P., & Henderson, G. (2017). Assessing ocean alkalinity for carbon sequestration. *Reviews of Geophysics*,
631 55(3), 636-674. <https://doi.org/https://doi.org/10.1002/2016rg000533>
- 632 Ringham, M. C., Hirtle, N., Shaw, C., Lu, X., Herndon, J., Carter, B. R., & Eisaman, M. D. (2024). An assessment
633 of ocean alkalinity enhancement using aqueous hydroxides: kinetics, efficiency, and precipitation
634 thresholds. *Biogeosciences*, 21(15), 3551-3570. <https://doi.org/https://doi.org/10.5194/bg-21-3551-2024>
- 635 Rogelj, J., Popp, A., Calvin, K. V., Luderer, G., Emmerling, J., Gernaat, D., Fujimori, S., Streffer, J., Hasegawa,
636 T., Marangoni, G., Krey, V., Kriegler, E., Riahi, K., van Vuuren, D. P., Doelman, J., Drouet, L., Edmonds,
637 J., Fricko, O., Harmsen, M.,...Tavoni, M. (2018). Scenarios towards limiting global mean temperature
638 increase below 1.5 °C. *Nature Climate Change*, 8(4), 325-332. <https://doi.org/10.1038/s41558-018-0091-3>
- 639 Sánchez, N., Goldenberg, S. U., Brüggemann, D., Jaspers, C., Taucher, J., & Riebesell, U. (2024). Plankton food
640 web structure and productivity under ocean alkalinity enhancement. *Science Advances*, 10(49), eado0264.
641 <https://doi.org/doi:10.1126/sciadv.ado0264>
- 642 Schulz, K. G., Bach, L. T., & Dickson, A. G. (2023). Seawater carbonate chemistry considerations for ocean
643 alkalinity enhancement research: theory, measurements, and calculations. *Guide to Best Practices in*
644 *Ocean Alkalinity Enhancement Research*, 2-oae2023, 2. <https://doi.org/10.5194/sp-2-oae2023-2-2023>
- 645 Schwinger, J., Bourgeois, T., & Rickels, W. (2024). On the emission-path dependency of the efficiency of ocean
646 alkalinity enhancement. *Environmental Research Letters*, 19(7). <https://doi.org/10.1088/1748-9326/ad5a27>
- 647 Sers, M. R., & Victor, P. A. (2018). The Energy-emissions Trap. *Ecological Economics*, 151, 10-21.
648 <https://doi.org/10.1016/j.ecolecon.2018.04.004>
- 649 Sjöberg, E. (1976). A fundamental equation for calcite dissolution kinetics. *Geochimica et Cosmochimica Acta*,
650 40(4), 441-447. [https://doi.org/https://doi.org/10.1016/0016-7037\(76\)90009-0](https://doi.org/https://doi.org/10.1016/0016-7037(76)90009-0)
- 651 Söhnle, O., & Mullin, J. W. (1988). Interpretation of crystallization induction periods. *Journal of colloid and*
652 *interface science*, 123(1), 43-50. [https://doi.org/https://doi.org/10.1016/0021-9797\(88\)90219-6](https://doi.org/https://doi.org/10.1016/0021-9797(88)90219-6)
- 653 Suessle, P., Taucher, J., Goldenberg, S., Baumann, M., Spilling, K., Noche-Ferreira, A., Vanharanta, M., &
654 Riebesell, U. (2023). Particle fluxes by subtropical pelagic communities under ocean alkalinity
655 enhancement. *EGUsphere*, 2023, 1-26. <https://doi.org/https://doi.org/10.5194/egusphere-2023-2800>
- 656 Suitner, N., Faucher, G., Lim, C., Schneider, J., Moras, C. A., Riebesell, U., & Hartmann, J. (2024). Ocean
657 alkalinity enhancement approaches and the predictability of runaway precipitation processes: results of
658 an experimental study to determine critical alkalinity ranges for safe and sustainable application
659 scenarios. *Biogeosciences*, 21(20), 4587-4604. <https://doi.org/10.5194/bg-21-4587-2024>
- 660 Tjørve, K. M., & Tjørve, E. (2017). The use of Gompertz models in growth analyses, and new Gompertz-model
661 approach: An addition to the Unified-Richards family. *PLoS One*, 12(6), e0178691.
662 <https://doi.org/https://doi.org/10.1371/journal.pone.0178691>
- 663 UNFCCC. (2015). Report of the Conference of the Parties to the United Nations Framework Convention on
664 Climate Change (21st Session, 2015: Paris). Retrived December. Vol. 4. 2015.



- 669 Varliero, S., Buono, A., Caserini, S., Raos, G., & Macchi, P. (2024). Chemical Aspect of Ocean Liming for CO₂
670 Removal: Dissolution Kinetics of Calcium Hydroxide in Seawater. *ACS Engineering Au.*
671 <https://doi.org/https://doi.org/10.1021/acsengineeringau.4c00008>
- 672 Wang, H., Pilcher, D. J., Kearney, K. A., Cross, J. N., Shugart, O. M., Eisaman, M. D., & Carter, B. R. (2023).
673 Simulated impact of ocean alkalinity enhancement on atmospheric CO₂ removal in the Bering Sea.
674 *Earth's Future*, 11(1). <https://doi.org/https://doi.org/10.1029/2022EF002816>
- 675 Wells, M. L., & Goldberg, E. D. (1992). Marine submicron particles. *Marine Chemistry*, 40(1-2), 5-18.
676 [https://doi.org/https://doi.org/10.1016/0304-4203\(92\)90045-C](https://doi.org/https://doi.org/10.1016/0304-4203(92)90045-C)
- 677 Wurgaft, E., Steiner, Z., Luz, B., & Lazar, B. (2016). Evidence for inorganic precipitation of CaCO₃ on suspended
678 solids in the open water of the Red Sea. *Marine Chemistry*, 186, 145-155.
679 <https://doi.org/https://doi.org/10.1016/j.marchem.2016.09.006>
- 680 Wurgaft, E., Wang, Z. A., Churchill, J. H., Dellapenna, T., Song, S., Du, J., Ringham, M. C., Rivlin, T., & Lazar,
681 B. (2021). Particle Triggered Reactions as an Important Mechanism of Alkalinity and Inorganic Carbon
682 Removal in River Plumes. *Geophysical Research Letters*, 48(11), 277.
683 <https://doi.org/https://doi.org/10.1029/2021gl093178>
- 684 Xin, X., Goldenberg, S. U., Taucher, J., Stühr, A., Aristegui, J., & Riebesell, U. (2024). Resilience of
685 Phytoplankton and Microzooplankton Communities under Ocean Alkalinity Enhancement in the
686 Oligotrophic Ocean. *Environ Sci Technol.* <https://doi.org/10.1021/acs.est.4c09838>
- 687 Zeebe, R., & Wolf-Gladrow, D. (2001). *CO₂ in Seawater: Equilibrium, Kinetics, Isotopes*. Elsevier Oceanography
688 Book Series. 65.
- 689 Zhong, S., & Mucci, A. (1989). Calcite and aragonite precipitation from seawater solutions of various salinities:
690 Precipitation rates and overgrowth compositions. *Chemical geology*, 78(3-4), 283-299.
691 [https://doi.org/https://doi.org/10.1016/0009-2541\(89\)90064-8](https://doi.org/https://doi.org/10.1016/0009-2541(89)90064-8)
- 692 Zhou, M., Tyka, M. D., Ho, D. T., Yankovsky, E., Bachman, S., Nicholas, T., Karspeck, A. R., & Long, M. C.
693 (2024). Mapping the global variation in the efficiency of ocean alkalinity enhancement for carbon dioxide
694 removal. *Nature Climate Change*, 1-7. <https://doi.org/https://doi.org/10.1038/s41558-024-02179-9>

695